

Information fusion and machine learning for sensitivity analysis using physics knowledge and experimental data

Berkcan Kapusuzoglu, Sankaran Mahadevan*

Department of Civil and Environmental Engineering, Vanderbilt University, TN 37235

Abstract

Sensitivity analysis is often performed using computational models of the physical phenomena; such models could be physics-based or data-driven, and the sensitivity estimate is affected by the accuracy and uncertainty of the physics model. If the physics-based computational model is expensive, an inexpensive surrogate model is built and used to compute the Sobol' indices in variance-based global sensitivity analysis (GSA), and the surrogate model introduces further approximation in the sensitivity estimate. This paper considers GSA for situations where both a physics-based model and a small number of experimental observations are available, and investigates strategies to effectively combine the two sources of information in order to maximize the accuracy and minimize the uncertainty of the sensitivity estimate. Physics-informed and hybrid machine learning strategies are proposed to achieve these objectives. Two machine learning (ML) techniques are considered, namely, deep neural networks (DNN) and Gaussian process (GP) modeling, and two strategies for incorporating physics knowledge within these ML techniques are investigated, namely: (i) incorporating loss functions in the ML models to enforce physics constraints, and (ii) pre-training and updating the ML model using simulation data and experimental data respectively. Four different models are built for each type (DNN and GP), and the uncertainties in these models are also included in the Sobol' indices computation. The DNN-based models, since they have many degrees of freedom in terms of model parameters, are found to result in smaller bounds on the sensitivity estimates when compared to the GP-based

*Corresponding author

Phone: 1-615-322-3040. Fax: 1-615-322-3365. Postal address: Vanderbilt University, VU Station B 356077, Nashville, TN 37235-6077, United States.

E-mail address: sankaran.mahadevan@vanderbilt.edu (S. Mahadevan).

models. The proposed methods are illustrated for an additive manufacturing example.

Keywords: Global sensitivity analysis, Sobol index, Deep learning, Physics-informed machine learning, Additive manufacturing, Fused filament fabrication

1. Introduction

Computational models are often used to predict the response of an engineering system since conducting experiments to directly measure the true response is often not feasible. However, the computational model is usually an incomplete representation of the complex physical system. In this case, the system response prediction is affected by the model uncertainty. The various sources of uncertainty are classified as (a) epistemic uncertainty due to lack of knowledge, and (b) aleatory uncertainty due to the inherent variability in the system or the external inputs. Global sensitivity analysis (GSA) [1] aims to provide a quantitative assessment of the relative contribution of each uncertainty source to the uncertainty in the model response [2–4].

Much of the GSA literature has focused on variability in the inputs and their effects on output variability; the extension of GSA to include epistemic uncertainty sources (data, model) is recent and sparse [5–7]. Model outputs can have uncertainty even for a fixed input when there exists model uncertainty. When the model is computationally expensive, it is often replaced with a surrogate model to facilitate the estimation of Sobol indices, since such computation requires many input-output samples from the model; the surrogate model introduces additional uncertainty. Several types of surrogate models are used in the literature, e.g., polynomial chaos expansion (PCE), Gaussian process regression, neural networks, etc., to train a parametric relationship between the inputs and the outputs. The quality and quantity of the training data affect the accuracy of these surrogate models, which directly affects the uncertainty in the model output [8–10]. Thus, it is important to also quantify the contribution of surrogate model uncertainty to the output uncertainty. In La Gratiot et al [8], the Gaussian process (GP) surrogate model uncertainty is included in the Sobol index estimates with a Monte Carlo procedure using multiple realizations of the GP model prediction, which helps to construct prediction intervals for the Sobol index estimates.

25 In high dimensional problems, the use of surrogate model-based GSA, which repeatedly exe-
 26 cutes the code by suppressing some variables and running through the range of other variables,
 27 may be an issue as the number of required number of executions of the code increases rapidly
 28 with the number of inputs [8, 11–13]. Expanding GSA to consider both aleatory and epistemic
 29 uncertainty is beneficial in supporting resource allocation decisions; if the contribution of epis-
 30 temic uncertainty is found to be significant, then it may be valuable to collect more data or
 31 refine the physics model to reduce the epistemic uncertainty and thus its contribution to the
 32 output uncertainty. Several GSA studies have developed auxiliary variable-based approaches to
 33 include both aleatory and epistemic uncertainty sources at a single level instead of using nested
 34 simulations, thus achieving both computational efficiency and direct ranking of the different
 35 sources of uncertainty. The auxiliary variable is used to transform one-to-many mapping to
 36 one-to-one mapping, thus facilitating the computation of Sobol indices for both aleatory and
 37 epistemic sources [14]. This idea is expanded in [15] to include several epistemic sources, such as
 38 input statistical uncertainty, surrogate model error, physics model discrepancy, and numerical
 39 solution error, and to systems with time series inputs and outputs.

40 Three scenarios of model and data availability can be considered for GSA: (1) use of a physics-
 41 based computational model, (2) use of available input-output data, either from experiments or
 42 previous simulations, or (3) use of both physics model and available input-output data. A
 43 straightforward model-based approach to estimate Sobol indices is to use a double-loop Monte
 44 Carlo simulation (MCS) [16]. In order to reduce the cost associated with the double-loop MCS,
 45 analytical and various efficient sample-based methods have been developed. The methodology
 46 developed by Sudret, which approximates the original physics model by a PCE and estimated
 47 the Sobol indices by post-processing the PCE coefficients [17]. The improved FAST method [18]
 48 combines the classical FAST method [2] with random balanced design [19] for generating samples
 49 to evaluate Sobol indices. Chen et al. [20] proposed analytical ways to compute Sobol’ indices
 50 for GP with input variables following normal or uniform distributions.

51 In some problems, input-output data may be already available instead of having to sim-
 52 ulate a physics model expressly for the purpose of GSA. Such data may be available from

53 experiments, from real-world observations, from Markov Chain Monte Carlo (MCMC) sampling
 54 during Bayesian model calibration, from MC sampling for reliability analysis, etc. In such cases,
 55 data-driven methods have been proposed to directly compute the Sobol indices based on avail-
 56 able input-output samples instead of simulation runs of the physics model [11, 21]. A GSA
 57 method based on ANOVA using factorial design of experiments is developed by Ginot et al. [22].
 58 The proposed method results in same values as the Sobol index since the variance decomposition
 59 used in the Sobol index estimations is same as the one used in the classical ANOVA [23]. The
 60 computational cost of most sample-based methods is proportional to the number of model input.
 61 Li and Mahadevan [24] proposed a modularized method, which has a computational cost that is
 62 not proportional to the model input dimension, to estimate the first-order Sobol indices based
 63 on stratification of available input-output samples. DeCarlo et al. [21] proposed an importance
 64 sampling approach by introducing weights to different data points to estimate Sobol indices
 65 from available data using Sobol' sequences to reduce the number of simulations. Probability
 66 model-based GSA have been recently proposed by Hu and Mahadevan [11] to estimate Sobol
 67 indices by building joint distribution models.

68 The third scenario is of interest in this paper, where both a physics-based model and some
 69 experimental or real-world data are available. One option, if adequate data is available, is to
 70 simply build a regression or machine learning (ML) model based on the observation data, and use
 71 this model to perform GSA. Multiple recent studies have pursued data-driven machine learning
 72 (ML) models in situations where abundant experimental data or real-world observations are
 73 available due to advances in modern sensing techniques. Generally, the construction of data-
 74 driven ML models does not require in-depth knowledge of the complex physics inherent in the
 75 physical process. ML models can learn complex systems using available observations, but the
 76 accuracy of these models depends on the quality and quantity of the data. If the available
 77 data is limited, then the complexity of the process cannot be captured. Further, since purely
 78 data-driven ML models do not explicitly consider physical laws, they can produce physically
 79 inconsistent results. In such cases, incorporating physics knowledge within ML models may
 80 improve the accuracy and efficiency of GSA computations. The combined use of physics-based

81 and ML models has been shown to achieve more accurate and physically consistent predictions
82 by leveraging the advantages of each method [25–27].

83 In this work, we incorporate physics knowledge into the ML models to better capture the
84 physics of the process by leveraging physical laws while improving the generalization performance
85 of data-driven models. Two types of ML models are considered in this paper, namely, GP and
86 DNN. Four different physics-informed machine learning (PIML) models are developed for each
87 type (i.e., GP or DNN) to predict the output quantity of interest (QoI), through combinations of
88 two strategies: (1) incorporating loss functions in the ML models to enforce physics constraints,
89 and (2) pre-training the ML model with simulation data and then updating it with experimental
90 data. The proposed methods can use multiple physics-based loss functions and enhance the data-
91 driven ML models to obey the physics laws. The resulting GSA includes the effect of uncertainty
92 in the ML or PIML model.

93 In summary, the contributions of this paper are as follows:

- 94 • Physics knowledge and experimental observations are fused in order to maximize the ac-
95 curacy and minimize the uncertainty of sensitivity estimates.
- 96 • Two PIML strategies and their combinations are investigated for sensitivity analysis using
97 both physics knowledge and experimental data.
- 98 • Four different models are built for both GP and DNN, and the uncertainties in these
99 models are included in the Sobol indices computation.
- 100 • The accuracy, uncertainty and computational effort for different options for ML and PIML
101 models are evaluated and compared.

102 The outline of the rest of this paper is as follows. Section 2 provides background information
103 on related methods. Section 3 presents the proposed methodology. The proposed methodology is
104 illustrated for a numerical example in Section 4. Concluding remarks are provided in Section 5.

2. Background

This section introduces each of the basic techniques used in developing the proposed methodology, namely variance-based GSA, Gaussian process surrogate modeling, and deep neural networks (DNN). These techniques are well established with extensive literature, therefore only a brief introduction is given here.

2.1. Probabilistic sensitivity analysis

Consider a deterministic real integrable one-to-one system response function $Y = f(\mathbf{X})$, where $f(\cdot)$ is the computational model, $\mathbf{X} = \{X_1, \dots, X_k\}$ are mutually independent model inputs, and Y is the model output. As shown by [16], the variance of Y can be decomposed as

$$V(Y) = \sum_i^k V_i + \sum_{i_1}^k \sum_{i_2=i_1+1}^k V_{i_1 i_2} + \sum_{i_1}^k \sum_{i_2=i_1+1}^k \sum_{i_3=i_2+1}^k V_{i_1 i_2 i_3} + \dots + V_{12\dots k} \quad (1)$$

where V_i is the variance of Y due to X_i alone, and $V_{i_1 \dots i_p} (p \geq 2)$ indicates the variance of Y due to $\{X_{i_1}, \dots, X_{i_p}\}$.

The Sobol indices are defined by dividing both sides of Eq. (1) with $V(Y)$

$$1 = \sum_i^k S_i + \sum_{i_1}^k \sum_{i_2=i_1+1}^k S_{i_1 i_2} + \sum_{i_1}^k \sum_{i_2=i_1+1}^k \sum_{i_3=i_2+1}^k S_{i_1 i_2 i_3} + \dots + S_{12\dots k} \quad (2)$$

where S_i is the first-order or main effects index that assesses the contribution of X_i individually to the variance of the output Y without considering interactions with other inputs. The higher-order indices $S_{i_1 \dots i_p} (p \geq 2)$ in Eq. (2) measure the contributions of the interactions among $\{X_{i_1}, \dots, X_{i_p}\}$.

The evaluation of S_i is defined as follows:

$$S_i = \frac{V_i}{V(Y)} = \frac{V_{X_i}(E_{\mathbf{X}_{-i}}(Y|X_i))}{V(Y)} \quad (3)$$

where \mathbf{X}_{-i} are all the model inputs other than X_i .

119 The overall contribution of X_i considering an individual input and its interactions with all
 120 other inputs is measured by the total effects index S_i^T :

$$S_i^T = 1 - \frac{V_{-i}}{V(Y)} = \frac{V_{\mathbf{X}_{-i}}(E_{x_i}(Y|\mathbf{X}_{-i}))}{V(Y)}. \quad (4)$$

121 The computation of S_i analytically is nontrivial since $E_{\mathbf{X}_{-i}}(\cdot)$ requires multi-dimensional
 122 integrals. A basic sampling-based approach is to use double-loop sampling [16]. One approach
 123 to reduce the computational cost is to replace the original computational model $f(\cdot)$ by a
 124 surrogate model and use this surrogate model in GSA with double-loop sampling [28–32]. A
 125 second approach is to use analytical solutions based on the coefficients of a polynomial chaos
 126 approximation [17]. A third approach is to pursue efficient single loop sampling techniques [24].

127 2.2. Gaussian process surrogate modeling

128 The GP surrogate model provides a prediction $G(\mathbf{u})$ at a given input \mathbf{u} as

$$G(\mathbf{u}) = \mathbf{h}(\mathbf{u})^T \boldsymbol{\beta} + Z(\mathbf{u}) \quad (5)$$

129 where $\mathbf{h}(\cdot)$ is the trend function, $\boldsymbol{\beta}$ is the vector of trend coefficients, and $Z(\cdot)$ is a zero-mean
 130 stationary GP which describes the deviation of the model from the trend. The covariance
 131 between the outputs $Z(\cdot)$ of the GP surrogate at points \mathbf{a} and \mathbf{b} is defined as:

$$\text{Cov}[Z(\mathbf{a}), Z(\mathbf{b})] = \sigma_Z^2 R(\mathbf{a}, \mathbf{b}) \quad (6)$$

132 where σ_Z^2 is the process variance and $R(\cdot, \cdot)$ is the correlation function. A squared exponential
 133 function with separated length scale parameters l_i for each input dimension has often been used
 134 in the literature:

$$R(\mathbf{a}, \mathbf{b}) = \exp \left[- \sum_{i=1}^M \frac{(a_i - b_i)^2}{l_i} \right] \quad (7)$$

The hyperparameters of the GP model, i.e., $\boldsymbol{\Theta} = \{l, \sigma_Z, \sigma_{obs}\}$, where σ_{obs} is the observation error, are inferred from the training data. A common method is to maximize the log marginal

likelihood function, which is defined as

$$\log p(\mathbf{Y}|\mathbf{X}; \boldsymbol{\Theta}) = -\frac{1}{2}\mathbf{Y}(\mathbf{K}_{TT} + \sigma_{obs}^2\mathbf{I})^{-1}\mathbf{Y} - \frac{1}{2}\log|\mathbf{K}_{TT} + \sigma_{obs}^2\mathbf{I}| + \frac{n}{2}\log 2\pi. \quad (8)$$

The outputs of the GP model are the mean prediction $\mu_G(\cdot)$ and the variance of the prediction $\sigma_G^2(\cdot)$, defined as:

$$\mu_G(\mathbf{u}) = \mathbf{h}(\mathbf{u})^T \boldsymbol{\beta} + \mathbf{r}(\mathbf{u})^T \mathbf{R}^{-1}(\mathbf{g} - \mathbf{F}\boldsymbol{\beta}) \quad (9)$$

$$\sigma_G^2(\mathbf{u}) = \sigma_Z^2 - \mathbf{A} \begin{bmatrix} \mathbf{0} & \mathbf{F}^T \\ \mathbf{F} & \mathbf{R} \end{bmatrix}^{-1} \mathbf{A}^T \quad (10)$$

where $\mathbf{r}(\mathbf{u})$ is a vector containing the covariance between \mathbf{u} and each of the training points $\{x_1, x_2, \dots, x_n\}$, $i \in \{1, \dots, n\}$, \mathbf{R} is an $n \times n$ matrix containing the correlation between each pair of training points, $\mathbf{R}(x_i, x_j) = \text{Cov}[Z(x_i), Z(x_j)]$; \mathbf{g} is the vector of original physics model outputs at each of the training points, \mathbf{F} is a $n \times q$ matrix with rows $\mathbf{h}(\mathbf{u}_i)^T$, and $\mathbf{A} = [\mathbf{h}(\mathbf{u})^T \mathbf{r}(\mathbf{u})^T]$.

2.3. Deep neural networks

In recent years, due to the confluence of advanced sensing and imaging techniques, big data processing techniques, and enormous computational power, rapid advances are being made in developing sophisticated data-driven machine learning models, particularly neural networks. A deep neural network (DNN) is composed of multiple hidden layers and has four major components: neuron, activation function, cost function, and optimization. Figure 1 shows a neural network consisting of three inputs, two hidden layers, each having four neurons, and two output neurons. The values of various input variables of a particular neuron are multiplied by their associated weights, then the sum of the products of the neuron weights and the inputs are calculated at each neuron. The summed value is passed through an activation function that maps the summed value to a fixed range before passing these signals on to the next layer of neurons.

The predictions of the DNN after a forward propagation, $\hat{\mathbf{Y}}$, are compared against the true response of the system, \mathbf{Y} , by defining a loss function (e.g., root mean squared error (RMSE)); $\mathcal{L}_{\text{RMSE}}(\mathbf{Y}, \hat{\mathbf{Y}}) = \sqrt{\sum_{i=1}^n (y_i - \hat{y}_i)^2 / n}$, which measures how far off the predictions are from the

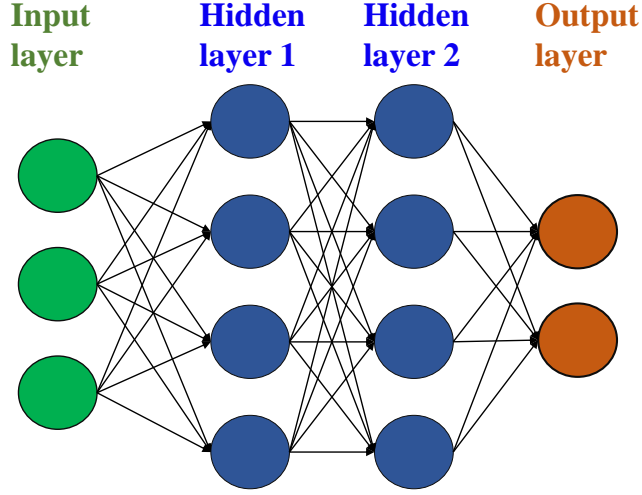


Fig. 1. A deep neural network with two hidden layers.

156 observations for the n training samples. After the forward propagation, backpropagation algo-
 157 rithms are employed to keep track of small perturbations to the weights that affect the error in
 158 the output and to distribute this error back through the network layers by computing gradients
 159 for each layer using the chain rule. In order to minimize the value of the loss function, necessary
 160 adjustments are applied at each iteration to the neuron weights in each layer of the network.
 161 These procedures are performed at each iteration until the loss function converges to a stable
 162 value.

163 3. Proposed methodology

164 The proposed methodology for sensitivity analysis using both physics knowledge and exper-
 165 imental data consists of the following steps:

- 166 1. PIML strategies
- 167 2. Implementation of PIML in GP
- 168 3. Implementation of PIML in DNN
- 169 4. Model uncertainty quantification in GP and DNN
- 170 5. Sobol indices computation with model uncertainty

171 The following subsections describe these steps in detail.

3.1. PIML strategies

PIML models seek to incorporate physics knowledge or constraints within the data-driven ML models. When a mechanistic, physics-based model is also available, complementary strengths of both mechanistic and ML models can be leveraged in a synergistic manner [27]. The aim is to improve the predictions beyond that of physics-based models or ML models alone by coupling physics-based models with ML models. Thus two different strategies to combine physics knowledge and ML models can be considered: (1) incorporate physics constraints in the ML models, and (2) pre-train and update the ML models using physics model input-output and experimental data, respectively.

3.1.1. Strategy 1: Enforcing physics constraints

A direct strategy to enforce physics constraints in ML model predictions is by including the constraints in the loss functions used in training the ML model [25]. Consider a PIML model with inputs \mathbf{X} and outputs $\hat{\mathbf{Y}}$ trained using physical laws that are incorporated as constraints into the loss function:

$$\mathcal{L} = \mathcal{L}_{\text{ML}} + \lambda_{\text{phy}} \mathcal{L}_{\text{phy}}(\hat{\mathbf{Y}}), \quad (11)$$

where \mathcal{L}_{ML} is the log marginal likelihood of the data for a GP model:

$$\mathcal{L}_{\text{GP}} = \log p(\mathbf{Y}|\mathbf{X}; \boldsymbol{\Theta}) \quad (12)$$

and regular training loss function for a DNN that evaluates a supervised error, e.g., root mean squared error (RMSE):

$$\mathcal{L}_{\text{DNN}}(\mathbf{Y}, \hat{\mathbf{Y}}) = \sqrt{\sum_{i=1}^n \frac{(Y_i - \hat{Y}_i)^2}{n}} \quad (13)$$

which measures the accuracy of predictions $\hat{\mathbf{Y}}$ for n training samples. The physics-based loss function \mathcal{L}_{phy} in the second term of Eq. 11 is weighted by a hyperparameter λ_{phy} ; the value of λ_{phy} controls the strength of the physics constraint enforcement. The inclusion of the second

term ensures physically consistent model predictions and helps to reduce the generalization error, which is a measure of how accurately a model is able to predict the output QoI for previously unseen data, even when there is a small amount of training data [25].

The physical inconsistencies in the model predictions are evaluated using the physics-based loss functions. The generic forms of these physical relationships can be expressed using the following constraints:

$$\begin{aligned}\mathcal{F}_1(\hat{\mathbf{Y}}, \mathbf{\Gamma}) &= 0, \\ \mathcal{F}_2(\hat{\mathbf{Y}}, \mathbf{\Gamma}) &\leq 0.\end{aligned}\tag{14}$$

where $\mathbf{\Gamma}$ denotes model parameters and physical variables. These equations can involve algebraic relationships or partial differentials of $\hat{\mathbf{Y}}$ and $\mathbf{\Gamma}$. The physics-based loss functions for these equations can be defined as:

$$\mathcal{L}_{\text{phy}}(\hat{\mathbf{Y}}) = \|\mathcal{F}_1(\hat{\mathbf{Y}}, \mathbf{\Gamma})\|^2 + \text{ReLU}(\mathcal{F}_2(\hat{\mathbf{Y}}, \mathbf{\Gamma})),\tag{15}$$

where $\text{ReLU}(x) = \max(0, x)$ represents the rectified linear unit function and it is used here to specify a quantitative range of operation, which penalizes when the difference between the predicted and target values are larger than the threshold, or to formulate a monotonic relationship for the QoI $\hat{\mathbf{Y}}$ [33].

3.1.2. Strategy 2: Pre-training and Updating

The model output accuracy and uncertainty are dependent on the quality and quantity of the available data. In some systems, the high cost associated with conducting experiments makes it infeasible to have adequate amount of training data to build purely data-driven models. Thus, it is important to effectively combine the physics-based model and a small amount of available experimental data in order to maximize the accuracy and minimize the uncertainty of the sensitivity estimate. When the experiments are expensive, they could only be conducted for a few values of the inputs, whereas it might be possible to run the physics-based model for

multiple combinations of input values. In that case, the simulation data can be used to pre-train an ML model, which is used as the initial model to be updated with experimental observations. Further, training of ML models requires the choice of initial values of the model parameters. The transfer of physical knowledge using a pre-trained ML model can prevent poor initialization due to lack of knowledge of initial choice of ML model parameters prior to training.

Since the pre-training based on the mechanistic model can use a large amount of training data (with multiple input parameter combinations) over a wide range of values, the pre-training may help the eventual ML model to have wider generalization beyond experimental data. In the numerical example in Section 4, the pre-training strategy exercises the physics model over 1310 input combinations, whereas only 39 experiments are available. However, if the physics model is computationally expensive, then the advantage of the pre-training strategy in using a larger input data set (from physics model runs) compared to the experiments becomes limited.

The two proposed strategies to predict the QoI are shown in Fig. 2. Figure 2(a) shows the first method, where the physical knowledge is included through constraints within the loss function of an ML trained with experimental data. Figure 2(b) shows the second method, where an ML model is first trained with data generated using the physics-based model and then updated using experimental data. The proposed PIML strategies can be applied to physical process by leveraging the related physical constraints or physics-based models.

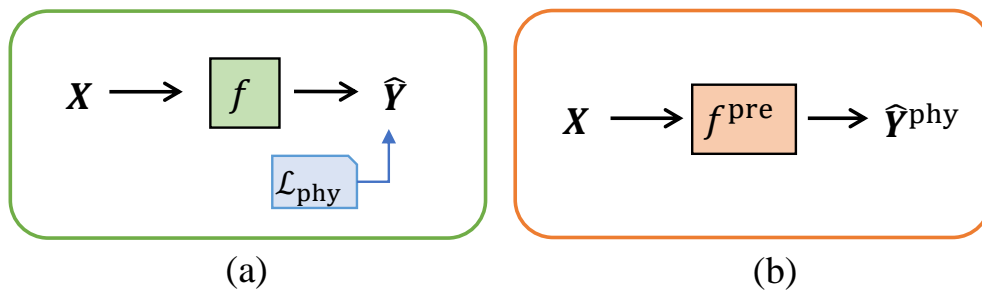


Fig. 2. PIML strategies: (a) incorporating physics-based loss functions in the ML models to enforce physics constraints, (b) pre-training an ML model with physics model input-output and updating it with experimental data.

3.2. Implementation of PIML strategies in GP and DNN

Based on the proposed two strategies to incorporate physics knowledge into the ML model, four separate ML models can be constructed for each type of surrogate model (GP and DNN):

- | | |
|---|--|
| 1. GP | 5. DNN |
| 2. $\text{GP}^{\mathcal{L}_{\text{phy}}}$ | 6. $\text{DNN}^{\mathcal{L}_{\text{phy}}}$ |
| 3. GP^{upd} | 7. DNN^{upd} |
| 4. $\text{GP}^{\text{upd}, \mathcal{L}_{\text{phy}}}$ | 8. $\text{DNN}^{\text{upd}, \mathcal{L}_{\text{phy}}}$ |

The following subsections describe the implementation of these models in detail.

3.2.1. Implementation of PIML in GP

In the first model, GP, only experimental observations are used for training. The hyperparameters are optimized during training by minimizing the error between the observations \mathbf{Y}_{obs} and GP model predictions $\mathbf{Y}_{\mathbf{m}}$. The difference between the true response of the system \mathbf{Y}_{true} and observations \mathbf{Y}_{obs} is attributed to observation error ϵ_{obs} , which is often treated as a zero-mean Gaussian random variable with variance σ_{obs}^2 .

Model 2 $\text{GP}^{\mathcal{L}_{\text{phy}}}$ incorporates the first strategy by enforcing physics constraints within the optimization of GP hyperparameters. More specifically, the physics constraints are incorporated into the maximization of the log marginal likelihood function (Eq. (8)) while inferring the hyperparameters of the GP model. Thus, the training of the second model is achieved by maximizing the following function:

$$\mathcal{L}_{\text{GP}} = \log p(\mathbf{Y}|\mathbf{X}; \boldsymbol{\Theta}) - \lambda_{\text{phy}} \mathcal{L}_{\text{phy}}(\hat{\mathbf{Y}}), \quad (16)$$

Model 3, GP^{upd} , where the second PIML strategy is pursued, pre-trains a GP surrogate model with data generated from the physics model, then improves the surrogate using experimental data. Consider a physics model f^{phy} that maps input variables \mathbf{X} and model parameters $\boldsymbol{\theta}_{\mathbf{m}}$ to

242 the numerical model output \mathbf{Y}_m :

$$\mathbf{Y}_m = \mathbf{G}(\mathbf{X}; \boldsymbol{\theta}_m(\mathbf{X})). \quad (17)$$

243 Let n_D be the number of collected observation data \mathbf{Y}_{obs} from experiments with input variables
 244 $\mathbf{x}^{(1)}, \dots, \mathbf{x}^{(n_D)}$, where $\mathbf{x}^{(i)}$ are the input variables for the i th experiment. There exists uncertainty
 245 in the model prediction due to missing physics or approximations as discussed in Section 1.
 246 Thus, a model discrepancy term $\boldsymbol{\delta}(\mathbf{X})$ as a function of model inputs is introduced to capture
 247 the missing information between \mathbf{Y}_{true} and \mathbf{Y}_m [34]. Thus, the true system response can be
 248 described as

$$\mathbf{Y}_{\text{true}}(\mathbf{X}) = \mathbf{Y}_{\text{obs}}(\mathbf{X}) + \epsilon_{\text{obs}}(\mathbf{X}) = \mathbf{Y}_m(\mathbf{X}) + \boldsymbol{\delta}(\mathbf{X}) = \mathbf{G}(\mathbf{X}; \boldsymbol{\theta}_m(\mathbf{X})) + \boldsymbol{\delta}(\mathbf{X}). \quad (18)$$

249 When the physics model $f^{\text{phy}}(\mathbf{X}) = \mathbf{Y}_m$ is computationally expensive, it is replaced by a
 250 cheaper surrogate model. In Model 3, a GP surrogate model $\text{GP}^{\text{phy}}(\mathbf{X}) = \hat{\mathbf{Y}}_m$ is used to ap-
 251 proximate the physics-based simulation model. The accuracy of the surrogate model prediction
 252 depends on the quality and quantity of the training data generated by the original physics model.
 253 The surrogate model error (ϵ_δ) can be incorporated as follows:

$$\mathbf{Y}_m(\mathbf{X}) = \hat{\mathbf{Y}}_m(\mathbf{X}) + \epsilon_\delta. \quad (19)$$

254 A common approach to estimate the discrepancy term is the one formulated by Kennedy and
 255 O’Hagan [34], which is applicable in the context of Bayesian calibration. In that case, physics
 256 model parameters are sought to be calibrated, and a discrepancy term is added in the calibration
 257 equation. The discrepancy term can be expressed in multiple ways, such as constant, Gaussian
 258 random variable with unknown parameters (either input-dependent or not), or Gaussian process
 259 (either stationary or non-stationary) [35]. The hyperparameters of the discrepancy term are then
 260 estimated along with the physics model parameters using Bayesian calibration. However, the
 261 situation considered here is much simpler. There is no calibration of physics model parameters

here; only the discrepancy term is needed. (In other words, the physics model parameters are already established). In that case, the model discrepancy can be evaluated for different input values of experimental tests and realizations of observation errors as follows:

$$\bar{\delta}(\mathbf{X}) = \mathbf{Y}_{\text{obs}}(\mathbf{X}) + \epsilon_{\text{obs}}(\mathbf{X}) - \hat{\mathbf{Y}}_m(\mathbf{X}). \quad (20)$$

where $\bar{\delta}(\mathbf{X}) = \delta(\mathbf{X}) + \epsilon_{\delta}$. In this work, a simplified approach is pursued by quantifying the overall model error instead of quantifying these error terms individually.

Following this, a GP model can be trained for the discrepancy term in terms of the inputs. Thus in model 3, two GP models are trained; (i) the first GP model ($\text{GP}^{\text{phy}}(\mathbf{X})$) replaces the physics model to predict the QoI; and (ii) the second GP model ($\text{GP}^{\text{exp}}(\mathbf{X})$) is constructed for the discrepancy term (i.e., the difference between the surrogate model prediction and real system) using experimental data.

The GP model for the model discrepancy ($\text{GP}^{\text{exp}}(\mathbf{X}) = \hat{\delta}$) captures the combined contribution of measurement error, physics and surrogate model errors for a given prediction. Thus, the predictions of the first GP model (pre-trained) are corrected/updated with the second GP model representing the model discrepancy term and can be written as

$$\hat{\mathbf{Y}}_{\text{corr}}(\mathbf{x}) = \hat{\mathbf{Y}}_m(\mathbf{X}) + \hat{\delta}. \quad (21)$$

Model 4 is a combination of the two strategies, in which both the pre-trained model is corrected with $\hat{\delta}$ and physics constraints are enforced.

3.2.2. Implementation of PIML in DNN

In model 5, a DNN is trained using only experimental data. In order to train the model, an optimization algorithm is used to find a set of model parameters (weights and biases) that best map inputs to outputs. Model 6 extends model by implementing the first strategy: physical knowledge related to the physical process is enforced through constraints within the loss function of the DNN, $\text{DNN}^{\mathcal{L}_{\text{phy}}}$ as shown in Eq. 11. The physics-based loss functions are evaluated for

284 given physics inputs at every optimization iteration of $\text{DNN}^{\mathcal{L}_{\text{phy}}}$.

285 Model 7 pursues the second strategy: where a DNN model is pre-trained using the coupled
 286 multi-physics model input-output DNN^{phy} and then updated with experimental data. The pre-
 287 trained model, f^{pre} , is first trained with physics model input-output data consisting of input
 288 parameter combinations over a range of experimental values. Then, the weights and biases of
 289 the pre-trained network, which are chosen as initial points in the optimization, are updated for
 290 different combinations of the proposed strategies using experimental data. Note that here the
 291 model parameters are updated in a least squares sense, whereas in GP (in model 3 GP^{upd} and
 292 4 $\text{GP}^{\text{upd}, \mathcal{L}_{\text{phy}}}$) a discrepancy term is assumed and updated using the experimental data.

293 Model 8 is a combination of the two strategies for DNN, where the initialization of the model
 294 parameters are obtained using the physics model input-output DNN^{phy} . These model parameters
 295 are updated during the training phase by minimizing the regular training loss function shown
 296 in Eq. 13 together with the physics-based loss functions that are given in Eq. 25.

297 3.3. Bayesian neural network

298 The estimates of the neural network model parameters (neuron weights \mathbf{w}) have uncertainty,
 299 and this uncertainty depends on the available training data. When the network's parameters
 300 are represented using distributions (to reflect the epistemic uncertainty) instead of deterministic
 301 values, the model is referred to as a Bayesian neural network (BNN) [36–38]. In this Bayesian
 302 context, the model parameter uncertainty is first described using a prior distribution $p(\mathbf{w})$, and
 303 the likelihood function is $p(\mathbf{Y}|\mathbf{X}, \mathbf{w})$. (A commonly used prior distribution is Gaussian, i.e.,
 304 $p(\mathbf{w} = \mathcal{N}(0, \mathcal{I}))$). Following Bayes' theorem, a posterior distribution over the model parameters
 305 given the training set $\{\mathbf{X}, \mathbf{Y}\} = \{\{\mathbf{x}_1, \dots, \mathbf{x}_N\}, \{\{\mathbf{y}_1, \dots, \mathbf{y}_N\}\}$ is defined by

$$p(\mathbf{w}|\mathbf{X}, \mathbf{Y}) = \frac{p(\mathbf{Y}|\mathbf{X}, \mathbf{w})p(\mathbf{w})}{p(\mathbf{Y}|\mathbf{X})}. \quad (22)$$

306 The Bayesian inference of the model outputs for a new input \mathbf{x}^* is given by the predictive

307 distribution as follows:

$$p(\mathbf{y}^*|\mathbf{x}^*, \mathbf{X}, \mathbf{Y}) = \int_{\Omega} p(\mathbf{y}^*|\mathbf{x}^*, \mathbf{w})p(\mathbf{w}|\mathbf{X}, \mathbf{Y})d\mathbf{w}. \quad (23)$$

308 The posterior distribution of model parameters $p(\mathbf{w}|\mathbf{X}, \mathbf{Y})$ is challenging to evaluate over the
 309 entire parameter space Ω due to the high dimensionality of Ω , and the highly non-linear behavior
 310 in the neural network caused by the non-linear activation functions and their combinations across
 311 multiple hidden layers.

312 Therefore, different approximate inference techniques can be considered to infer the posterior
 313 distribution $p(\mathbf{w}|\mathbf{X}, \mathbf{Y})$ [39–42]. One such approximation is variational inference, which fits a
 314 simple and tractable distribution $q_{\theta}(\mathbf{w})$ to the posterior, parametrized by a variational parameter
 315 θ [39]. This approximates the intractable problem by optimizing the parameters of $q_{\theta}(\mathbf{w})$.
 316 The closeness of the variational distribution is often measured by the Kullback-Leibler (KL)
 317 divergence between the approximate distribution $q_{\theta}(\mathbf{w})$ and the true model posterior $p(\mathbf{w}|\mathbf{X}, \mathbf{Y})$.

318 Dropout is a regularization approach which helps reducing interdependent learning amongst
 319 the neurons; thus prevents over-fitting. The term *dropout* refers to randomly dropping out
 320 neurons with a given dropout rate during the training phase in a neural network. A Monte
 321 Carlo (MC) dropout technique has been developed in recent years [43] which is equivalent to
 322 performing approximate variational inference. In MC dropout, dropout is not only applied
 323 while training a model but also during prediction. Randomly chosen neurons are temporarily
 324 removed from the network along with their connections. Next, the gradients of neurons weights
 325 are calculated on a sub-neural network for each training data and these gradients are then
 326 averaged over the training sets to obtain the weights of overall network. The optimization
 327 of Bayesian neural networks to find the optimal model parameters with the MC dropout is
 328 equivalent to using dropout (only during training) as regularization—modification made to the
 329 model in order to reduce its generalization error—on neural networks. However, in contrast to
 330 standard neural networks, the MC dropout performs dropout and generates random samples
 331 following a Bernoulli distribution for each neuron in the input and hidden layers during testing.

332 The neuron that takes the value 0 is dropped out with a given dropout probability p_d . The
 333 outputs of the network are predicted using the collection of generated random samples from the
 334 posterior predictive distribution and the uncertainty in the prediction of a new data is quantified
 335 with the trained network.

336 The MC dropout strategy provides an efficient way of Bayesian inference to quantify the
 337 model prediction uncertainty, and can be applied to a variety of neural networks, such as feed-
 338 forward neural networks, convolutional neural networks, and recurrent neural networks [44].

339 3.4. Sobol indices computation with model uncertainty

340 As discussed earlier, often in physics-based and data-driven models it is necessary to quantify
 341 the model uncertainty and its contribution to the Sobol index estimates. In this section, we
 342 present the inclusion of model uncertainty in the Sobol index estimates.

Every surrogate model has uncertainty in the prediction. In a noise free model, the GP predictions at the training points have zero variance and at any other points the variance is non-zero. The prediction at any point is given by a normal distribution with a mean and variance. The uncertainty inherent in these predictions can be captured by sampling, which can be then used in GSA. The model uncertainty pertaining to the GP model is propagated to the Sobol index estimations using the following estimator (see [8]):

$$S_{m,n}^{X_{d_1}} = \frac{V_{m,n}^{X_{d_1}}}{V_{m,n}} = \frac{\frac{1}{m} \sum_k Z_n(X_k) Z_n(\bar{X}_k) - \frac{1}{m} \sum_k Z_n(X_k) \frac{1}{m} \sum_k Z_n(\bar{X}_k)}{\frac{1}{m} \sum_k Z_n(X_k)^2 - \left(\frac{1}{m} \sum_k Z_n(X_k)\right)^2}, \quad (24)$$

343 where Z is the Gaussian process and (X, \bar{X}) are the random vectors.

344 The distribution of $S_{m,n}^{X_{d_1}}$ can be obtained as follows:

Algorithm 1: Estimation of the distribution

1. Build $Z_n(x)$

Result: Write here the result
initialization;

while *While condition* **do**

instructions;

if *condition* **then**

instructions1;

instructions2;

else

instructions3;

end

end

I WILL COMPLETER THIS ALGORITHM TOMORROW.

A similar approach is implemented to the DNN models with the use of MC dropout (with a given dropout rate). However, in contrast to GP models, the samplings are different in DNN models. In DNN models, we randomly set units of the network to zero and generate posteriors using MC dropout. Whereas, we sample from a multivariate normal distribution in GP models to quantify the uncertainty in the Sobol index estimates with prediction intervals.

Two types of ML models were considered, namely, GP and DNN models, for GSA by effectively fusing physics knowledge and experimental data to maximize the accuracy and minimize the uncertainty of the sensitivity estimates. Eight different PIML models were developed by leveraging the two strategies described above. The effect of ML model uncertainty on the Sobol index estimates is quantified using the algorithm described above.

4. Numerical illustration

An additive manufacturing application is used to illustrate the proposed PIML models for GSA and compare their performance. A commercial material Ultimaker Black Acrylonitrile butadiene styrene (ABS) was extruded from an Ultimaker 2 Extended+ 3D printer to manu-

360 facture fused filament fabrication (FFF) parts with unidirectionally aligned filaments and then
361 measured with appropriate diagnostic techniques. FFF is a widely used additive manufacturing
362 (AM) process due to its easy operation, low cost and suitability for complex geometries. As
363 the molten filament is deposited layer upon layer through a nozzle, it cools down, solidifies
364 and bonds with the surrounding filaments. Rectangular ABS amorphous polymer specimens of
365 length 35 mm, width 12 mm, and thickness 4.2 mm are manufactured with constant filament
366 height, width and length (0.7, 0.8, and 35 mm, respectively).

367 The output quantity of interest is porosity of the printed part, and the inputs are two process
368 parameters, namely nozzle temperature and speed. The porosity of an FFF part is dependent
369 on the temperature history at the interfaces between filaments. Thus, it is important to predict
370 the temperature evolution of filaments for estimating the final mesostructure of the printed
371 part. The analytical solution proposed by Costa et al. [45] for transient heat transfer during the
372 printing process in FFF is used to predict the temperature evolution of filaments. A physics-
373 based sintering model is developed, which considers realistic filament geometry, and allows the
374 filament geometry to change during the printing process. This model is used to predict the
375 porosity of the FFF part using the temperature evolution of filaments, material properties,
376 part geometry, and process parameters as inputs. Thus the mapping from input to output is a
377 multi-physics model, i.e., models of two physical phenomena (heat transfer and sintering) are
378 combined to predict the porosity given the extrusion temperature and extrusion speed.

379 The statistical properties of the QoI are observed to have negligible variability along the
380 length of the specimens; thus the porosity measurements were taken at the midpoint of each part
381 with the use of microscopy images processed through the ImageJ software [46]. Filaments were
382 extruded through a nozzle with 0.8 mm diameter. The build plate temperature was constant and
383 set to 110°C. Using Latin hypercube sampling, 39 sets of process parameters \mathbf{X} were generated.
384 The ranges considered for the two process variables were: printer extrusion temperature T :
385 (210°C - 260°C), and extrusion speed S : (15 mm/s - 46 mm/s).

 The basic ML models, namely Model 1 (for GP) and Model 5 (for DNN) are simply trained
with the 39 sets of process inputs (temperature and speed) and output (porosity). In the training

of Model 2 $\text{GP}^{\mathcal{L}_{\text{phy}}}$ and Model 6 $\text{DNN}^{\mathcal{L}_{\text{phy}}}$, we impose two physics-based loss functions (i.e., two separate physics relationships, $\mathcal{L}_{\text{phy},k}(\hat{\mathbf{Y}})$, where $k = \{1, 2\}$ and $\hat{\mathbf{Y}}$ is the porosity prediction). The physical inconsistencies in the model predictions are evaluated using the physics-based loss functions defined as follows:

$$\begin{aligned}\mathcal{L}_{\text{phy},1}(\hat{\mathbf{Y}}) &= \frac{1}{N} \sum_{i=1}^N \text{ReLU}(-\hat{Y}_i), \\ \mathcal{L}_{\text{phy},2}(\hat{\mathbf{Y}}) &= \frac{1}{N} \sum_{i=1}^N \text{ReLU}(\hat{Y}_i - \phi_{0,i}),\end{aligned}\tag{25}$$

where these loss functions consider the physical violations related to the porosity across N samples. In the first loss function, negative values of porosity are treated as physical violations. The second loss function penalizes the model when the predicted final porosity \hat{Y}_i is greater than the initial porosity $\phi_{0,i}$ of i th part. This is based on the physics knowledge that the total void area decreases as the bond formation takes place. Thus, the porosity predictions are ensured to be physically meaningful with the inclusion of these physics-based penalty functions.

In Model 3 GP^{upd} and Model 7 DNN^{upd} , the ML models are pre-trained using the multi-physics model input-output. The pre-trained ML models are then updated using the experimental data. The training data for pre-training consists of 1310 input parameter combinations over a range of experimental values, i.e., ($210^\circ\text{C} \leq T \leq 260^\circ\text{C}$, $15 \text{ mm/s} \leq S \leq 46 \text{ mm/s}$). (Note that there are only 39 physical experiments are available; this is one of the advantages of this pre-training/updating strategy, where the pre-training can be over a much larger set of input combinations, thus improving the generalization performance of the updated model). The input data are normalized prior to the training of the ML models (the output quantity porosity is dimensionless and between 0 and 1),

Model 4 $\text{GP}^{\text{upd}, \mathcal{L}_{\text{phy}}}$, which is a combination of the two strategies for DNN and uses the model parameters obtained through the physics model input-output as the initial values. Then, during the training of the updating phase these parameters are updated by minimizing the following loss function:

Following this, a GP model can be trained for the discrepancy term in terms of the inputs.

Thus in model 3, two GP models are trained; (i) the first GP model ($\text{GP}^{\text{phy}}(\mathbf{X})$) replaces the physics model to predict the QoI; and (ii) the second GP model ($\text{GP}^{\text{exp}}(\mathbf{X})$) is constructed for the discrepancy term (i.e., the difference between the surrogate model prediction and real system) using experimental data.

Model 4 is a combination of the two strategies for GP, in which two GP models are trained; (i) the first GP model ($\text{GP}^{\text{phy}}(\mathbf{X})$) trained using the physics model input-output samples; and (ii) the second GP model ($\text{GP}^{\text{exp}}(\mathbf{X})$) is built for the discrepancy term using the experimental data while maximizing the following function to optimize the hyperparameters of $\text{GP}^{\text{exp}}(\mathbf{X})$:

$$\mathcal{L}_{\overline{\text{GP}}} = \mathcal{L}_{\text{GP}} + \lambda_{\text{phy}}^{\text{GP}} \mathcal{L}_{\text{phy}}(\hat{\mathbf{Y}}). \quad (26)$$

Model 8 $\text{DNN}^{\text{upd}, \mathcal{L}_{\text{phy}}}$, which is a combination of the two strategies for DNN, uses the model parameters obtained through the physics model input-output as the initial values. Then, during the training of the updating phase these parameters are updated by minimizing the following loss function:

$$\mathcal{L}_{\overline{\text{DNN}}} = \mathcal{L}_{\text{DNN}} + \lambda_{\text{phy}}^{\text{DNN}} \mathcal{L}_{\text{phy}}(\hat{\mathbf{Y}}). \quad (27)$$

The computational cost of different models for training and estimation of Sobol indices based on 5000 MC samples with a fixed number of experimental data ($n = 39$) is given in Table. 1. The time it takes for training and computation of Sobol indices using GP models 2-4 is significantly greater than model 1, i.e., 2-5 minutes. The difference becomes even greater when the number of observations increase. The reason for the difference between the training time of GP and GP^{upd} is the pre-training phase, where a large amount of physics input-output samples used. Whereas, the difference between the training time of GP and $\text{GP}^{\mathcal{L}_{\text{phy}}}$ due to the inclusion of physics constraints, which makes it harder for the optimization to find optimal hyperparameters. Whereas, the computation time for training of each DNN model is on average 15 sec using a desktop computer (Intel® Xeon® CPU E5-1660 v4@3.20GHz with 32 GB RAM and GPU NVIDIA Quadro K620 with 2 GB) and the Sobol index estimations based on 5000

421 samples take approximately 1-2 minutes for DNN models (models 5-8).

Table 1

Computational effort of eight models for training and estimation of first-order and total-effect Sobol indices using 5000 MC samples with $n = 39$ number of observations.

Models	Training time [in minutes]	Evaluation of the distribution of $S_{m,n}^{X_{d_1}}$ [in minutes]
GP	< 1	3
GP \mathcal{L}_{phy}	2	5
GP ^{upd}	3	7
GP ^{upd} , \mathcal{L}_{phy}	4	8
DNN	< 1	1
DNN \mathcal{L}_{phy}	< 1	2
DNN ^{upd}	< 1	2
DNN ^{upd} , \mathcal{L}_{phy}	1	2

4.1. GSA using GP models

423 The Sobol index computations with the GP models (1-4) are based on 5000 MC samples
424 and 100 realizations of the Gaussian process. The hyperparameters of models 2 (GP \mathcal{L}_{phy}) and 4
425 (GP^{upd}, \mathcal{L}_{phy}) are assumed to be ($\lambda_{\text{phy}}^{\text{GP}} = 50, 50$). The standard deviation of the observation error
426 is assumed to be 0.001.

427 The effect of number of observations in the first-order Sobol index estimates of temperature
428 for the first four models are illustrated in Fig. ???. The mean values of $S_{m,n}^{X_{d_1}}$ based on the GP
429 model predictions are denoted with solid dots at given number of observations n . The 95% pre-
430 diction intervals are represented with bars above and below the solid dots for the corresponding
431 model.

432 The prediction intervals decrease as more number of experimental data used to train the
433 models. Further, all four models converge to similar first-order and total-effect sensitivity esti-
434 mates for both printer extrusion temperature and speed. The relative contribution of printer
435 extrusion speed to the variability of the porosity (≈ 0.65) is greater than printer extrusion
436 temperature (≈ 0.25).

4.2. GSA using DNN models

438 The four DNN models (Models 5 to 8) were implemented using the Keras package [47] with
439 Tensorflow in the backend. The hyperparameters of models 6 (DNN \mathcal{L}_{phy}) and 8 (DNN^{upd}, \mathcal{L}_{phy})

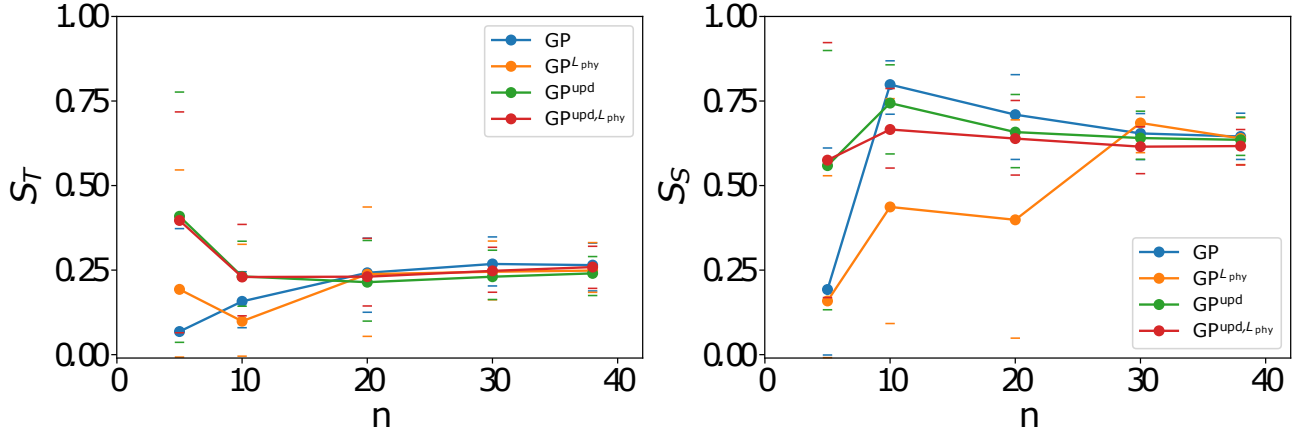


Fig. 3. First-order sensitivity index estimators for: (a) printer extrusion temperature, and (b) speed using GP models.

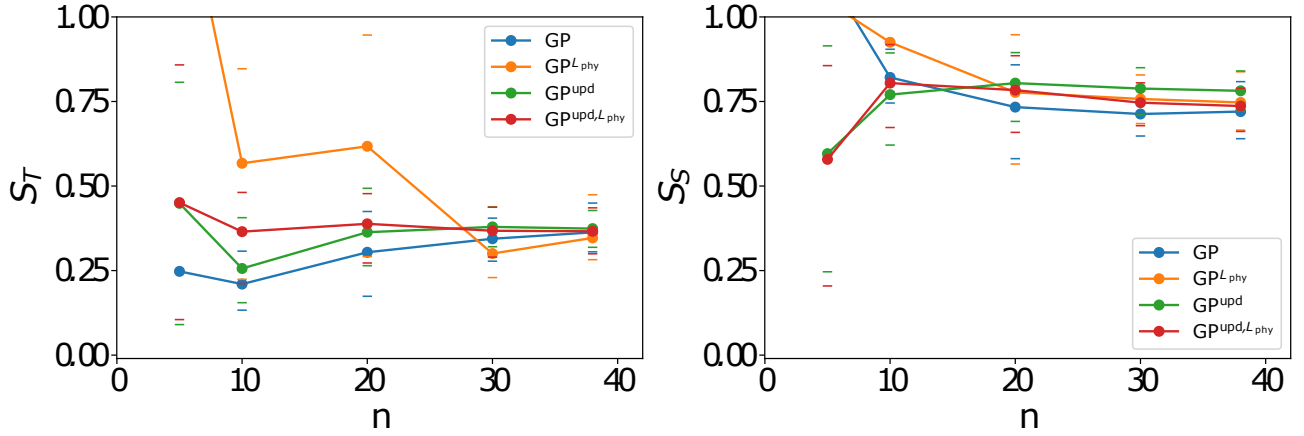


Fig. 4. Total-effect sensitivity index estimates for: (a) printer extrusion temperature, and (b) speed using GP models.

are tuned with grid search ($\lambda_{\text{phy}}^{\text{DNN}} = 0.15, 0.15$). Fully-connected DNN models with 2 hidden layers and 5 neurons in each hidden layer are constructed. The Rectified Linear Unit (ReLU) activation function and Adam optimizer are used to perform stochastic gradient descent in learning the model parameters.

4.2.1. GSA using DNN models without MC dropout

The DNN models without MC dropout maps deterministic inputs to a deterministic output. Therefore, unique Sobol index values are obtained. These unique values based on the DNN model predictions are represented with solid dots for different number of observations $n = 5, 10, 20, 30, 38$.

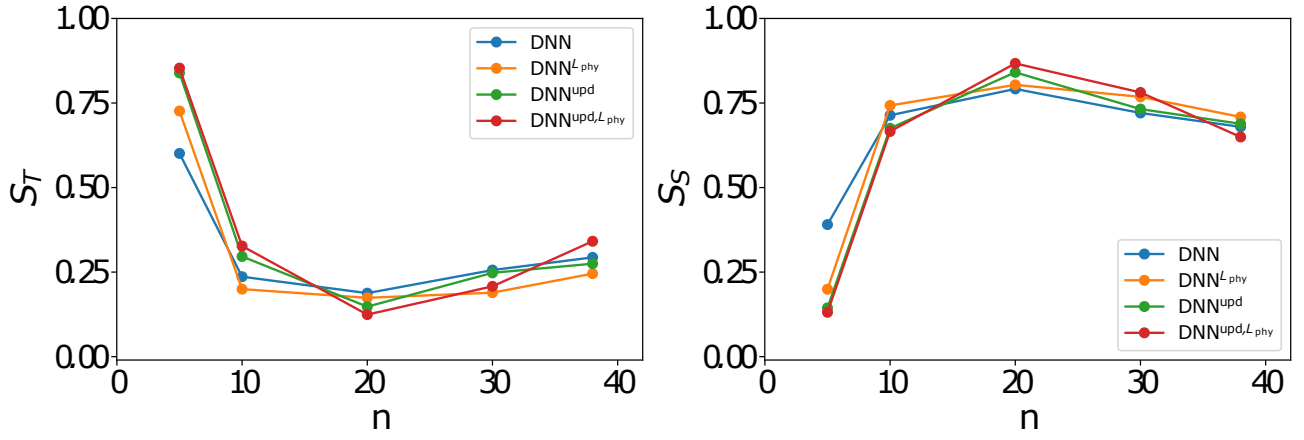


Fig. 5. First-order sensitivity index estimators for: (a) printer extrusion temperature, and (b) speed using DNN models.

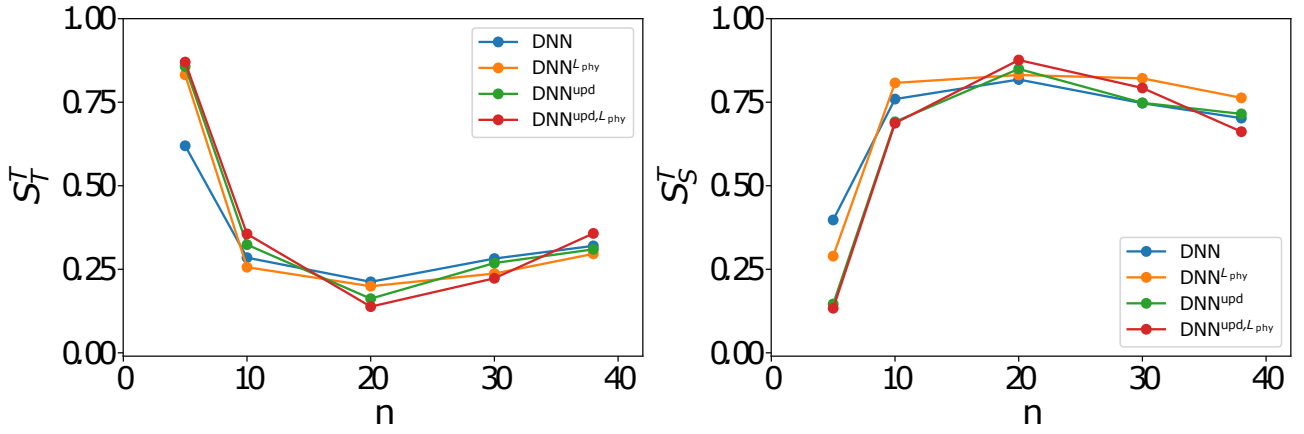


Fig. 6. Total-effect sensitivity index estimates for: (a) printer extrusion temperature, and (b) speed using DNN models.

All DNN models converge to similar first-order and total-effect sensitivity estimates for both input parameter and these values are consistent with the results obtained using GP models. The main difference between the results obtained using GP and DNN models is that the sensitivity estimates evaluated based on the DNN model predictions do not show a strong convergence, which may be because of the noisy data or the quality of the data.

4.2.2. GSA using DNN models with MC dropout

DNN models with MC dropout results in bounds for the sensitivity estimates as opposed to DNN models without MC dropout. The mean values of $S_{m,n}^{X_{d_1}}$ MC dropout predictions are represented with solid dots based on 100 stochastic forward passes through the networks for

different number of observations. The 95% prediction intervals are represented with bars above and below the solid dots for the corresponding model.

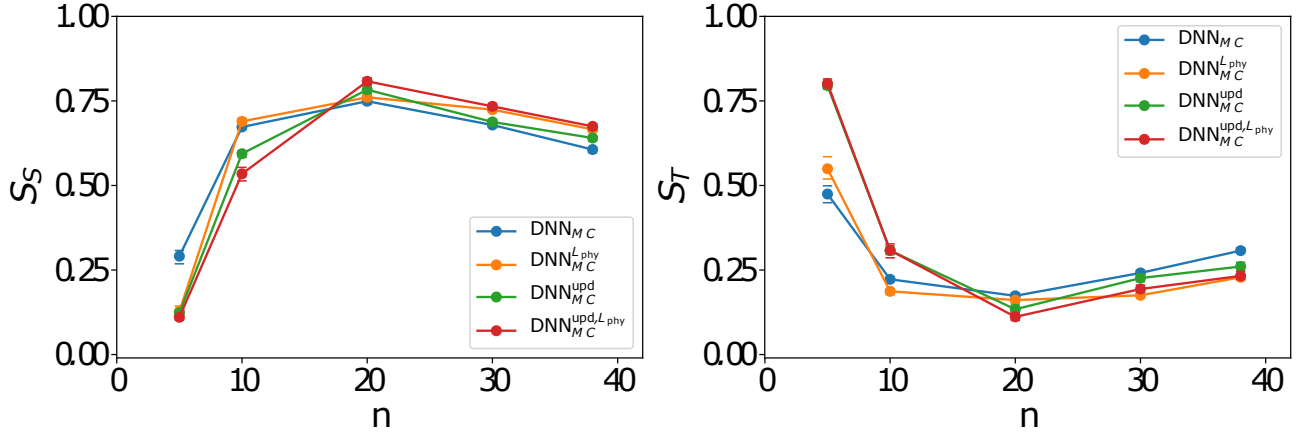


Fig. 7. First-order sensitivity index estimators for: (a) printer extrusion temperature, and (b) speed using DNN models with MC dropout.

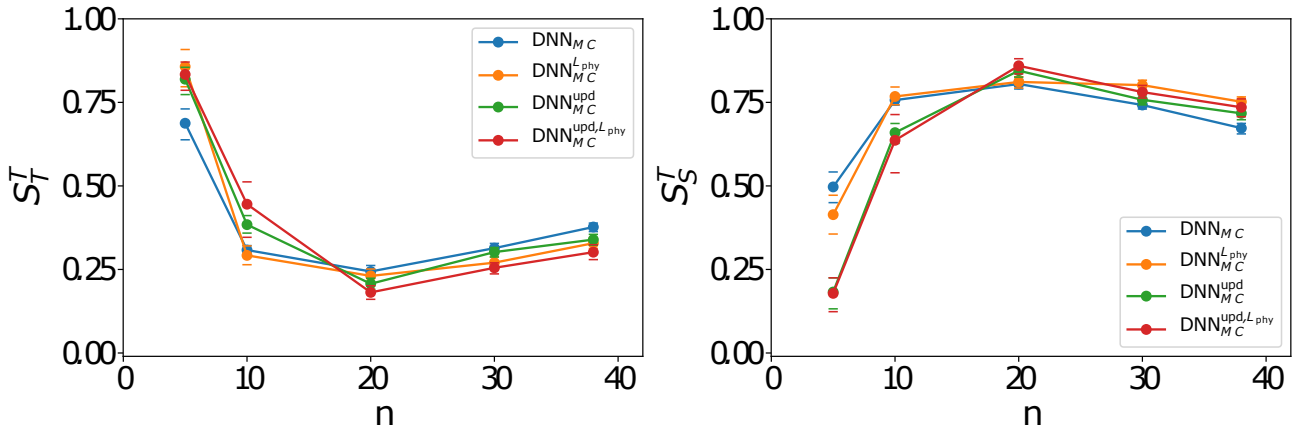


Fig. 8. Total-effect sensitivity index estimates for: (a) printer extrusion temperature, and (b) speed using DNN models with MC dropout.

The optimized dropout rate p_d used for the MC dropout simulations is 0.05. All four models converge to similar first-order and total-effect sensitivity estimates for both printer extrusion temperature and speed. The relative contribution of printer extrusion speed to the variability of the porosity (≈ 0.65) is greater than printer extrusion temperature (≈ 0.25). The MC dropout results converge to similar values obtained using the DNN models without MC dropout. Further, the prediction intervals decrease as more number of experimental data used to train the models and they are significantly smaller than the ones obtained using GP models.

467 The effect of dropout rate p_d for a fixed number of observations ($n=38$) in the first-order
 468 Sobol index estimates of DNN models using MC dropout is shown in Fig. 9. The total-effect
 469 Sobol index estimates of DNN models using MC dropout with different dropout rates for $n = 38$
 470 is given in Fig. 10. The values of first-order and total-effect sensitivity index obtained using DNN
 471 models with MC dropout for printer extrusion temperature, and speed increase with increasing
 472 dropout rates except the range (0.0-0.025). These results show that the dropout rate is also
 473 needed to be optimized together with the other hyperparameters to be able to achieve accurate
 sensitivity estimates.

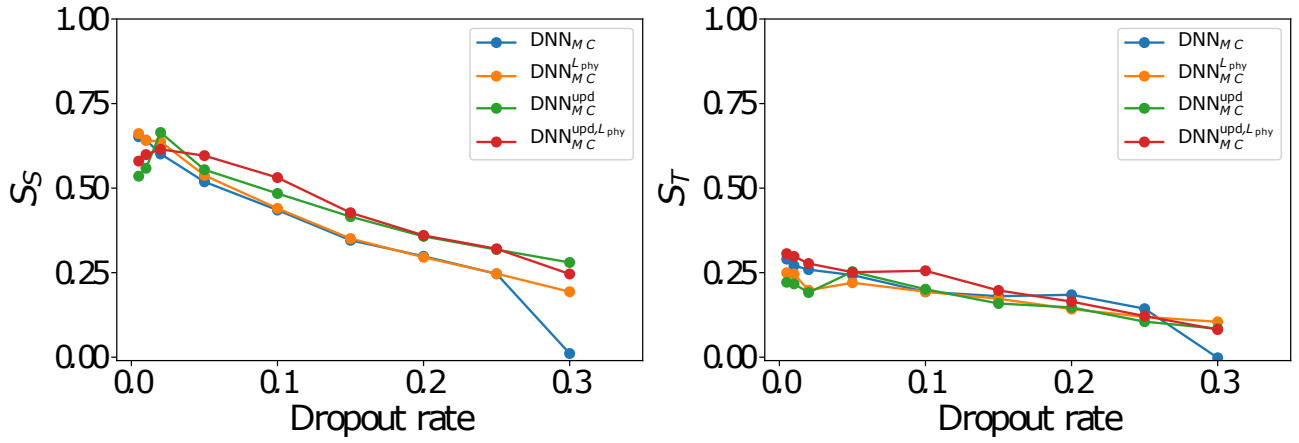


Fig. 9. First-order sensitivity index estimators for: (a) printer extrusion temperature, and (b) speed using DNN models with MC dropout.

474

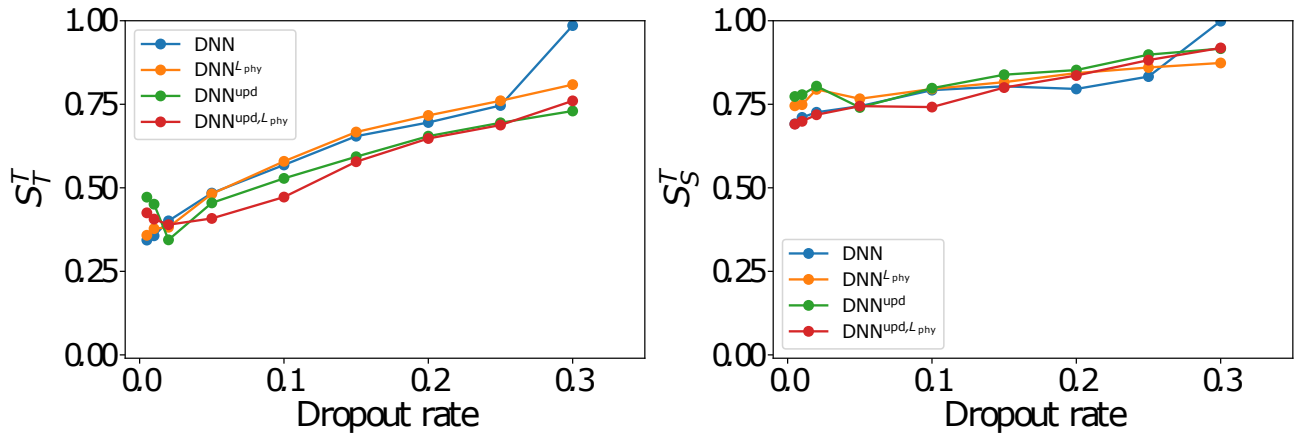


Fig. 10. Total-effect sensitivity index estimates for: (a) printer extrusion temperature, and (b) speed using DNN models with MC dropout.

475 5. Conclusion

476 In this paper, methodologies for information fusion and machine learning for sensitivity
477 analysis using physics knowledge and experimental data while accounting for model uncertainty
478 were developed. Variance-based sensitivity analysis is used to quantify the relative contribution
479 of uncertainty source to the variability of the output quantity. Two types of ML models were
480 considered, namely, GP and DNN models. Several PIML models were developed by leverag-
481 ing two strategies for incorporating physics knowledge into ML models: (1) incorporating loss
482 functions in the ML models to enforce physics constraints, and (2) pre-training an ML model
483 with simulation data and then updating it with experimental data. The effect of ML model
484 uncertainty on the sensitivity index estimate is analyzed, and the accuracy and computational
485 of the various PIML models are compared.

486 The results show that the application of PIML strategies to both GP and DNN allows accu-
487 rate Sobol index computations even with smaller amounts of experimental data while producing
488 physically meaningful results. Thus, the proposed approach helps to fill the physics knowledge
489 gap in the ML models while estimating the Sobol indices accurately by correcting for the ap-
490 proximation in the physics-based models. Numerical examples studied show that training the
491 GP models for estimating the Sobol indices require more computational effort than the DNN
492 models.

493 In future work, the proposed framework needs to be tested for problems with a larger number
494 of dimensions both in the input and output, with multiple combinations to further analyze the
495 convergence of Sobol index estimates for different PIML strategies. Future work can also explore
496 the weighting of the two sources of data since the data produced by physics-based models and
497 experiments have different levels of credibility.

498 References

- 499 [1] A. Saltelli, M. Ratto, T. Andres, F. Campolongo, J. Cariboni, D. Gatelli, M. Saisana,
500 S. Tarantola, Global sensitivity analysis: the primer, John Wiley & Sons, 2008.

- [2] A. Saltelli, S. Tarantola, K.-S. Chan, A quantitative model-independent method for global sensitivity analysis of model output, *Technometrics* 41 (1) (1999) 39–56.
- [3] T. A. Mara, S. Tarantola, Variance-based sensitivity indices for models with dependent inputs, *Reliability Engineering & System Safety* 107 (2012) 115–121.
- [4] E. Borgonovo, E. Plischke, Sensitivity analysis: a review of recent advances, *European Journal of Operational Research* 248 (3) (2016) 869–887.
- [5] C. Liang, S. Mahadevan, Bayesian framework for multidisciplinary uncertainty quantification and optimization, in: 16th AIAA Non-Deterministic Approaches Conference, 2014, p. 1499.
- [6] C. Liang, S. Mahadevan, S. Sankararaman, Stochastic multidisciplinary analysis under epistemic uncertainty, *Journal of Mechanical Design* 137 (2) (2015).
- [7] Z. Hu, S. Mahadevan, Uncertainty quantification in prediction of material properties during additive manufacturing, *Scripta materialia* 135 (2017) 135–140.
- [8] L. Le Gratiet, C. Cannamela, B. Iooss, A bayesian approach for global sensitivity analysis of (multifidelity) computer codes, *SIAM/ASA Journal on Uncertainty Quantification* 2 (1) (2014) 336–363.
- [9] J. E. Oakley, A. O’Hagan, Probabilistic sensitivity analysis of complex models: a bayesian approach, *Journal of the Royal Statistical Society: Series B (Statistical Methodology)* 66 (3) (2004) 751–769.
- [10] A. Marrel, B. Iooss, B. Laurent, O. Roustant, Calculations of sobol indices for the gaussian process metamodel, *Reliability Engineering & System Safety* 94 (3) (2009) 742–751.
- [11] Z. Hu, S. Mahadevan, Probability models for data-driven global sensitivity analysis, *Reliability Engineering & System Safety* 187 (2019) 40–57.

- 524 [12] A. Marrel, B. Iooss, F. Van Dorpe, E. Volkova, An efficient methodology for modeling
525 complex computer codes with gaussian processes, *Computational Statistics & Data Analysis*
526 52 (10) (2008) 4731–4744.
- 527 [13] A. O’Hagan, Bayesian analysis of computer code outputs: A tutorial, *Reliability Engineer-*
528 *ing & System Safety* 91 (10-11) (2006) 1290–1300.
- 529 [14] S. Sankararaman, S. Mahadevan, Separating the contributions of variability and parameter
530 uncertainty in probability distributions, *Reliability Engineering & System Safety* 112 (2013)
531 187–199.
- 532 [15] C. Li, S. Mahadevan, Relative contributions of aleatory and epistemic uncertainty sources
533 in time series prediction, *International Journal of Fatigue* 82 (2016) 474–486.
- 534 [16] I. M. Sobol, Global sensitivity indices for nonlinear mathematical models and their monte
535 carlo estimates, *Mathematics and computers in simulation* 55 (1-3) (2001) 271–280.
- 536 [17] B. Sudret, Global sensitivity analysis using polynomial chaos expansions, *Reliability engi-*
537 *neering & system safety* 93 (7) (2008) 964–979.
- 538 [18] S. Tarantola, D. Gatelli, T. A. Mara, Random balance designs for the estimation of first
539 order global sensitivity indices, *Reliability Engineering & System Safety* 91 (6) (2006) 717–
540 727.
- 541 [19] F. Satterthwaite, Random balance experimentation, *Technometrics* 1 (2) (1959) 111–137.
- 542 [20] W. Chen, R. Jin, A. Sudjianto, Analytical variance-based global sensitivity analysis in
543 simulation-based design under uncertainty (2005).
- 544 [21] E. C. DeCarlo, S. Mahadevan, B. P. Smarslok, Efficient global sensitivity analysis with
545 correlated variables, *Structural and Multidisciplinary Optimization* 58 (6) (2018) 2325–
546 2340.

- 547 [22] V. Ginot, S. Gaba, R. Beaudouin, F. Aries, H. Monod, Combined use of local and anova-
548 based global sensitivity analyses for the investigation of a stochastic dynamic model: ap-
549 plication to the case study of an individual-based model of a fish population, *Ecological*
550 *modelling* 193 (3-4) (2006) 479–491.
- 551 [23] G. Archer, A. Saltelli, I. Sobol, Sensitivity measures, anova-like techniques and the use of
552 bootstrap, *Journal of Statistical Computation and Simulation* 58 (2) (1997) 99–120.
- 553 [24] C. Li, S. Mahadevan, An efficient modularized sample-based method to estimate the first-
554 order sobol’ index, *Reliability Engineering & System Safety* 153 (2016) 110–121.
- 555 [25] A. Karpatne, W. Watkins, J. Read, V. Kumar, Physics-guided neural networks (pgnn): An
556 application in lake temperature modeling, *arXiv preprint arXiv:1710.11431* (2017).
- 557 [26] X. Jia, J. Willard, A. Karpatne, J. S. Read, J. A. Zwart, M. Steinbach, V. Kumar, Physics-
558 guided machine learning for scientific discovery: An application in simulating lake temper-
559 ature profiles, *arXiv preprint arXiv:2001.11086* (2020).
- 560 [27] J. Willard, X. Jia, S. Xu, M. Steinbach, V. Kumar, Integrating physics-based modeling
561 with machine learning: A survey, *arXiv preprint arXiv:2003.04919* (2020).
- 562 [28] L. L. Gratiet, S. Marelli, B. Sudret, Metamodel-based sensitivity analysis: polynomial chaos
563 expansions and gaussian processes, *arXiv preprint arXiv:1606.04273* (2016).
- 564 [29] A. Marrel, B. Iooss, S. Da Veiga, M. Ribatet, Global sensitivity analysis of stochastic
565 computer models with joint metamodels, *Statistics and Computing* 22 (3) (2012) 833–847.
- 566 [30] D. Xiu, G. E. Karniadakis, The wiener–askey polynomial chaos for stochastic differential
567 equations, *SIAM journal on scientific computing* 24 (2) (2002) 619–644.
- 568 [31] A. Janon, M. Nodet, C. Prieur, Uncertainties assessment in global sensitivity indices esti-
569 mation from metamodels, *International Journal for Uncertainty Quantification* 4 (1) (2014).

- [32] Z. Hu, X. Du, Mixed efficient global optimization for time-dependent reliability analysis, *Journal of Mechanical Design* 137 (5) (2015).
- [33] N. Muralidhar, M. R. Islam, M. Marwah, A. Karpatne, N. Ramakrishnan, Incorporating prior domain knowledge into deep neural networks, in: 2018 IEEE International Conference on Big Data (Big Data), IEEE, 2018, pp. 36–45.
- [34] M. C. Kennedy, A. O’Hagan, Bayesian calibration of computer models, *Journal of the Royal Statistical Society: Series B (Statistical Methodology)* 63 (3) (2001) 425–464.
- [35] Y. Ling, J. Mullins, S. Mahadevan, Selection of model discrepancy priors in bayesian calibration, *Journal of Computational Physics* 276 (2014) 665–680.
- [36] J. S. Denker, Y. LeCun, Transforming neural-net output levels to probability distributions, in: *Advances in neural information processing systems*, 1991, pp. 853–859.
- [37] D. J. MacKay, A practical bayesian framework for backpropagation networks, *Neural computation* 4 (3) (1992) 448–472.
- [38] R. M. Neal, *Bayesian learning for neural networks*, Vol. 118, Springer Science & Business Media, 2012.
- [39] C. Blundell, J. Cornebise, K. Kavukcuoglu, D. Wierstra, Weight uncertainty in neural networks, *arXiv preprint arXiv:1505.05424* (2015).
- [40] A. Graves, Practical variational inference for neural networks, in: *Advances in neural information processing systems*, 2011, pp. 2348–2356.
- [41] J. M. Hernández-Lobato, Y. Li, M. Rowland, D. Hernández-Lobato, T. Bui, R. Turner, Black-box α -divergence minimization (2016).
- [42] Y. Gal, Z. Ghahramani, Bayesian convolutional neural networks with bernoulli approximate variational inference, *arXiv preprint arXiv:1506.02158* (2015).

- 593 [43] Y. Gal, Z. Ghahramani, Dropout as a bayesian approximation: Representing model un-
594 certainty in deep learning, in: international conference on machine learning, 2016, pp.
595 1050–1059.
- 596 [44] X. Zhang, S. Mahadevan, Bayesian neural networks for flight trajectory prediction and
597 safety assessment, Decision Support Systems (2020) 113246.
- 598 [45] S. Costa, F. Duarte, J. Covas, Estimation of filament temperature and adhesion develop-
599 ment in fused deposition techniques, Journal of Materials Processing Technology 245 (2017)
600 167–179.
- 601 [46] C. A. Schneider, W. S. Rasband, K. W. Eliceiri, Nih image to imagej: 25 years of image
602 analysis, Nature methods 9 (7) (2012) 671.
- 603 [47] F. Chollet, et al., keras. github repository, <https://github.com/fchollet/keras>. Accessed
604 on 25 (2015) 2017.